

The following publication Cheung, T. -, Hong, L., Rao, N., Yang, C., Wang, L., Lai, W. J., . . . Yong, K. -. (2016). The non-aqueous synthesis of shape controllable Cu<sub>2-x</sub>S plasmonic nanostructures in a continuous-flow millifluidic chip for the generation of photo-induced heating. *Nanoscale*, 8(12), 6609-6622 is available at <https://doi.org/10.1039/C5NR09144F>.



## Nanoscale

### PAPER

# Non-aqueous synthesis of shape controllable Cu<sub>2-x</sub>S plasmonic nanostructures in a continuous-flow millifluidic chip for the generation of photo-induced heating

Received 00th January 20xx,  
Accepted 00th January 20xx

DOI: 10.1039/x0xx00000x

[www.rsc.org/](http://www.rsc.org/)

Tai-Lok Cheung,<sup>†ab</sup> Liying Hong,<sup>†b</sup> Nanxi Rao,<sup>a</sup> Chengbin Yang,<sup>b</sup> Libo Wang,<sup>c</sup> Wenn Jing Lai,<sup>c</sup> Peter Han Joo Chong,<sup>\*b</sup> Wing-Cheung Law<sup>\*a</sup> and Ken-Tye Yong<sup>\*b</sup>

In this paper, a new method for synthesizing non-aqueous copper sulfide nanocrystals with different shapes and sizes using a homemade continuous-flow millifluidic chip is presented. Conventionally, shape control of nanocrystals was accomplished using a surfactant-controlled approach, where directional growth is facilitated by selective passivation of a particular facet of the nanocrystals using surfactants. We demonstrate a “surfactant-free” approach where different sizes and shapes (i.e. spherical, triangular prism and rod) of plasmonic copper sulfide (Cu<sub>2-x</sub>S) nanocrystals can be fabricated by adjusting the flow rate and precursor concentrations. As continuous-flow synthesis enables uniform heating and easy variation of precursors’ stoichiometries, it serves as an excellent incubation platform for nanoparticles due to its simplicity and high reproducibility. Transmission electron microscope (TEM), fast Fourier transform (FFT) and X-ray diffraction (XRD) techniques were used to characterize the as-synthesized nanocrystals and revealed that structures ranging from copper-deficient covellite (CuS), spionkopite (Cu<sub>1.35</sub>S), roxbyite (Cu<sub>1.75</sub>S), to copper-rich djurleite (Cu<sub>1.94</sub>S). The localized surface plasmon resonance (LSPR) peak of the nanocrystals can be tuned from 1115 to 1644 nm by simply varying the copper to sulfur molar ratio and flow rate. Furthermore, photothermal effect of Cu<sub>2-x</sub>S nanocrystals were also demonstrated to annihilate the RAW264.7 cells upon near infra-red laser irradiation.

## Introduction

Size control of nanostructured materials, which are important for a wide range of applications ranging from bioimaging to nanoelectronic devices, has become a hot research topic over the past decade. The optical and electrochemical properties of nanoparticles (NPs) (e.g. localized surface plasmon resonance (LSPR)) as well as their performance in applications, were primarily determined by the shape and monodispersity of NPs. Highly monodispersed NPs with well-defined size, shape, morphology and surface functionalized chemistry, offer sensitive optical responses and high selectivity in targeting diseased cells which are of paramount importance in biophotonics and nanomedicine.

Traditionally, NPs were commonly synthesized using the bench-top system. In general, this system is a macro-scale synthesis platform which consists of magnetic stirring/sonication and a temperature controller, which aims to provide a homogenous distribution of thermodynamic energy for nucleation and growth of NPs. However, these macroscale actuators generally create a broad distribution of kinetic energies resulting in temperature differences within the reaction chamber. The agitation performance of the sonicator simulated by Tsai and Song et al. showed that the chamber geometry, immersion depth of the ultrasonic probe, agitation time, frequency and power setting of the sonicator, have considerable effects on the heat generated, flow velocity and pressure inside the reaction chamber.<sup>1,2</sup> The agitation frequency and temperature could vary significantly in different parts of the incubation chamber, thereby generating varying precursor reactivities within the system. The varied reactivity of precursors then caused the NPs to be formed with different stoichiometric ratios leading to variation of structures and morphologies of the NPs and polydispersity within the same batch.

On the other hand, there are many instances of NP fabrication using flow synthesis. One of major categories is continuous-flow microfluidic synthesis. Monodispersed nanoparticles can be fabricated due to precise sequential

<sup>a</sup> Department of Industrial and Systems Engineering, The Hong Kong Polytechnic University, Hung Hom, Kowloon, Hong Kong SAR, P. R. China. E-mail: roy.law@polyu.edu.hk.

<sup>b</sup> School of Electrical and Electronic Engineering, Nanyang Technological University, 50 Nanyang Avenue, 639798, Singapore. E-mail: ktyong@ntu.edu.sg, ehichong@ntu.edu.sg

<sup>c</sup> AOMC

<sup>d</sup> Temasek Laboratories@NTU, Nanyang Technological University, 50 Nanyang Drive, Singapore 637553, Singapore

<sup>†</sup> These authors contributed equally to this work.

<sup>††</sup> Electronic Supplementary Information (ESI) available. See DOI: 10.1039/x0xx00000x

addition of the precursors downstream on the chip and uniform temperature distribution.<sup>3</sup> In addition, since the input kinetic energy can be easily tuned by varying the flow rates, size-tunable nanoparticles such as Au,<sup>4,5</sup> CdS,<sup>6</sup> Fe<sub>3</sub>O<sub>4</sub>,<sup>7</sup> and CdSe,<sup>8,9</sup> can be achieved. Other continuous-flow studies have also shown that properties such as the crystal/phase of the nanoparticles can be altered,<sup>10</sup> magnetic intensity can be enhanced<sup>11</sup> and the reduced full-width-half-maximum of the fluorescent emission.<sup>12</sup> Even the complex core-shell CdSe/ZnS can be produced using the simple continuous-flow microfluidic synthesis.<sup>13</sup> However, there are many instances which exposes the disadvantages for microfluidic chip synthesis such as the sophisticated operational control, time consuming fabrication, relatively low throughput rate and fabrication cost.<sup>14-16</sup> Another alternative for flow synthesis is the millifluidic chip fabrication. Millifluidic synthesis is gathering interest among researchers for the fabrication of NPs such as Cu nanoclusters, Cu and Fe<sub>2</sub>O<sub>3</sub>.<sup>16-18</sup> Millifluidics boasts comparative advantages like ease-of-fabrication, high throughput rate and suitability for other applications such as radiation-based X-ray absorption spectroscopy<sup>15,19</sup> aside from similar advantages as microfluidics such as uniform heating and interaction time between precursors. At the same time, empirical research have shown that the continuous-flow millifluidic synthesis is capable of controlling the size of NP such as Ag and Au as well.<sup>15,20,21</sup> Interestingly, this method of flow synthesis provides another dimension besides size control. C. J. Murphy's group has recently reported the shape and size control of Au nanoparticles synthesized using the continuous-flow millifluidic chip,<sup>19</sup> while R. Tadmouri's group have also shown shape control of metallic NPs in multi-phase millifluidic synthesis.<sup>22</sup> In addition, the relative large channel sizes can enhance the production rate and throughput rate, thus enabling scaled-up production.<sup>23,24</sup>

The millifluidic on-chip fabrication method provides many other advantages for NP formation similar to microfluidic synthesis. For example, it provided a larger surface area to volume ratio so that uniform heating can be achieved during the entire synthesis process.<sup>25</sup> Song and Liu suggested that the winding channel design and multiphase mixing can be used to enhance the precursors' reaction.<sup>26,27</sup> In addition, using continuous-flow approach to fabricate NPs could ensure a well-maintained stoichiometry ratio between the precursors since laminar flow in the engineered channels provides a constant interface for fluid interaction.<sup>28</sup> Moreover, the millifluidic on-chip fabrication could also provide a more precise control of the reaction time. This is a crucial parameter in obtaining the desired sizes of NPs as the reaction can be quenched desirably after propagating through a certain length of channel. By making use of this distance-to-time control, the properties of the NPs can be fine-tuned and engineered for specific sensing and imaging applications. Therefore, the millifluidic on-chip fabrication technique provides an excellent means for precise fabrication of NPs. This miniaturized reaction platform opens up opportunities for synthesizing a wide range of NPs in a well-controlled manner. In fact, due to the high surface-to-volume of the channels on the chip, the temperature can be raised quickly within a short period of time, enabling uniform heating and

rapid nucleation of NPs. This makes millifluidic on-chip NP fabrication more favorable and functional for organic phase synthesis. However, the field of organic phase synthesis of NPs in continuous-flow synthesis is just in its infancy stages with only several reports mostly documenting CdSe quantum dots (QDs) synthesis.<sup>8,9,12,13</sup> Interestingly, high quality QDs could be produced by employing the continuous-flow regime during synthesis, in which the growth mechanism was in sharp contrast to the conventional "hot injection" in bench-top approach. More importantly, to allow for a continuous-flow process, the system should be open but no specific "de-gassing" progress was required. It seemed that conducting chemical reactions in a tiny volume on the chip not only offered advantages of controllable laminar flow, uniform heating, complete mixing and small amount of required solvent, but also provided an oxygen-free environment without requiring any active controls.

In order to explore the capabilities of continuous-flow millifluidic in organic phase synthesis, we demonstrated the shape and size control of Cu<sub>2-x</sub>S nanocrystals (NCs) using a continuous-flow millifluidic chip in this paper. The Cu<sub>2-x</sub>S NCs were chosen in this study because Cu<sub>2-x</sub>S emerged as novel plasmonic NCs which have a large range of carrier (hole) densities extending from 1017 to 1023 cm<sup>-3</sup> and relatively high thermal conductivities, making them attractive for photovoltaics, biophotonics, single molecular detection and disease therapy.<sup>29-32</sup> We found that by varying the flow rates and copper to sulfur molar ratio, different sizes and shapes of Cu<sub>2-x</sub>S NCs could be produced. The photothermal effect obtained from these NCs could then be used to annihilate RAW264.7 cells upon near infra-red (NIR) laser irradiation.

## Experimental

### Materials

Copper (I) chloride (99.995%, Sigma Aldrich), sulfur (analytical grade, Sigma Aldrich), oleylamine (>50.0%, Tokyo Chemical Industry Co., Ltd.), oleic acid (>85.0%, Tokyo Chemical Industry Co., Ltd.), toluene (>99.5%, Tokyo Chemical Industry), chloroform (ACS standard, Merck Pte Ltd), and absolute ethanol (≥99.5 %, Merck Pte Ltd) were used in the synthesis of the nanoparticles. The 184 Sylgard silicone elastomer kit from Dow Corning was used to fabricate the polydimethylsiloxane (PDMS) continuous-flow millifluidic chip. RAW264.7 mice macrophage cell line (ATCC, Manassas, VA, USA), Dulbecco's Modified Eagle's Medium ([DMEM], Hyclone), fetal bovine serum ([FBS], Hyclone), penicillin-streptomycin (Gibco, Life Technologies, SG, Singapore) were used in cell culturing, while cell viability was determined using the MTT (3-(4,5-dimethylthiazol-2-yl)-2,5-diphenyltertrazolium-bromide) assay kit (Sigma Aldrich), dimethylsulfoxide ([DMSO], Sigma Aldrich) and Apoptosis Detection Kit I (BD Pharmingen, San Diego, USA). All chemicals were used as received without further purification. Deionized (DI) water mentioned in the experiments was purified by a Milli-Q water purification system.

### Fabrication of Millifluidic chip for Continuous-Flow Synthesis

The polydimethylsiloxane (PDMS) mixture was obtained by mixing the base resin and the curing agent in the volume ratio of 1:10 using the 184 Sylgard silicone elastomer kit bought from Dow Corning. A 3D printer from PP3DP and the software SketchUp was used to design and print the device mould using the material acrylonitrile butadiene styrene (ABS). The PDMS mixture is poured onto the ABS mould and to form the device after 4 hours of heat curing at around 65°C. The cured PDMS layer with the channels was then removed from the printed plastic ABS mould and carefully bonded to a glass slide. Holes were punched at the inlets of the PDMS chip and polytetrafluoroethylene (PTFE) tubes were inserted to deliver the precursors into the chip. Therefore, such a method is a convenient, inexpensive and easy way to fabricate the PDMS chip with reasonably precise dimensions and reproducibility.

### Continuous-Flow Synthesis of Cu<sub>2-x</sub>S NCs

The synthesis protocol used in this experiment is similar to previous report.<sup>33</sup> Briefly, sulfur (1 mmol, 6 mmol or 10 mmol) was dissolved in 10 ml of oleic acid (OA) and heated at 120°C with stirring. Similarly, copper (I) chloride (1 mmol, 6 mmol or 10 mmol) was dissolved in 10 ml of oleylamine (OAm) and also heated at 120°C with stirring for 30 minutes. After 30 minutes, the temperature of the copper-oleylamine (Cu-OAm) mixture was raised to 200°C and then cooled to 120°C before withdrawing the mixture using a syringe. The sulfur-oleic acid (S-OA) mixture was also likewise withdrawn in the syringe. The PDMS chip was pre-heated at 120°C on a hot plate and the two precursor mixtures were subsequently simultaneously injected into the chip in a continuous-flow using a syringe pump (KD Scientific). The precursors were well-mixed in the initial winding section to initiate the nucleation process, while the subsequent straight section allowed the growth of the particles. Lastly, the Cu<sub>2-x</sub>S NCs were quenched by adding absolute (99%) ethanol near the end of the channels. The mixture was centrifuged at 8000 rpm for 2 minutes and redispersed in chloroform.

In order to investigate the growth of the Cu<sub>2-x</sub>S<sub>2</sub> particles were synthesized at different flow rates (150 µl/min, 1000 µl/min, 2000 µl/min, 3000 µl/min, 4000 µl/min and 5000 µl/min) with constant copper to sulfur ratio (1:2). In addition, Cu<sub>2-x</sub>S particles with different copper to sulfur molar ratios (1:10, 1:6, 1:2, 2:1, 6:1 and 10:1) under the same flow rate (3000 µl/min) were also studied.

### Characterization of Cu<sub>2-x</sub>S NCs

Transmission electron microscope (TEM) images were captured using a JEOL JEM-2011 TEM. UV-vis-NIR absorbance spectra were measured using a PerkinElmer Lambda 950 UV/Vis/NIR Spectrophotometer System. Powdered X-ray diffraction (XRD) measurements were obtained using the Rigaku SmartLab powder XRD diffractometer.

### Ligand Exchange to L-glutathione (GSH) capped Cu<sub>2-x</sub>S NCs

The Cu<sub>2-x</sub>S NCs were synthesized and dispersed in organic solvents and thus had to undergo ligand exchange with GSH to allow the nanocrystal to be in the aqueous phase. This would enable biocompatibility for subsequent uptake into the cells. 1 mmol of reduced GSH was dissolved in 1 mL of DI water with the pH of the solution adjusted to pH 10-11 by adding an appropriate amount of NaOH solution. Following that, 1 mL of the as-synthesized Cu<sub>2-x</sub>S NCs dispersed in chloroform was added to the mixture. The reaction mixture was then stirred vigorously for 30 minutes with simultaneous addition of absolute ethanol. Lastly, the mixture was centrifuged at 8000 rpm for 2 minutes and redispersed in DI water.

### Cell Culture

RAW264.7 mice macrophage cells (American Type Culture Collection) were cultured with Dulbecco's modified eagle's medium (DMEM, Hyclone), supplemented with 10% FBS, penicillin (100 µg/mL, Gibco) and streptomycin (100 µg/mL, Gibco) in a humidified environment with 37°C and 5% CO<sub>2</sub> inside an incubator.

### Cytotoxicity

The RAW264.7 cells were seeded at a density of 1 × 10<sup>4</sup> cells/well into the 96-well plate and allowed to adhere for 24 hours. The macrophage cells were then treated with different concentrations of the GSH capped Cu<sub>2-x</sub>S NCs for another 24 hours. Cell viability was studied using the MTT (3-(4,5-dimethylthiazol-2-yl)-2,5-diphenyltertrazolium bromide) assay kit (Sigma). 20 µL of 5 mg/mL MTT in phosphate buffered saline (PBS) was added to each well and incubated for another 4 hours. Then, the precipitate was dissolved in 150 µL of 100% dimethylsulfoxide (DMSO, Sigma) with gentle shaking. Absorbance readings were measured using a microplate reader (Bio-Rad) at 490 nm wavelength. The cell viability was obtained by normalizing the absorbance of the sample wells with the control well and expressed as percentages, taking the viability of untreated cells as 100%.

### Cellular Uptake of GSH capped Cu<sub>2-x</sub>S NCs and NIR Laser Illumination

The cells were seeded in a 6-well plate seeded at a density of 1 × 10<sup>5</sup> cells/well with DMEM culture medium. Based on the MTT cytotoxicity studies, 13.5 µM and 27 µM concentrations were added to the macrophage cells. After 4 hours of incubation, the treated cells were rinsed thrice with PBS buffer (pH = 7.2). A multimode fiber coupled diode laser (K915FA3RN-30.00W, BWT Beijing Ltd.) with centre wavelength of 915 ± 10 nm and a numerical aperture (NA) of 0.22 with a straight cleaved fiber end was used to illuminate the cells with near infra-red (NIR) laser light. The output optical power was adjusted to attain different power densities for cell illumination. Each spot was exposed to the NIR laser light with a fixed power density for 15 minutes.

### *In vitro* Cell Imaging

After illumination, the cells were placed in the incubator for 30 minutes. The FITC Annexin V Apoptosis Detection Kit I (BD Pharmingen, San Diego, USA) was used to carry out the apoptosis assay according to the manufacturer's protocol.<sup>34</sup> Briefly, the cells were washed twice with cold PBS and suspended in the binding buffer. Then 5  $\mu\text{L}$  of FITC Annexin V and 5  $\mu\text{L}$  of propidium iodide (PI) were added and gently swirled before incubating for another 15 minutes at room temperature in the dark. A fluorescence microscope (Eclipse-Ti, Nikon) was used for *in vitro* cell imaging. Damaged or dead cells were stained with PI and emitted red fluorescence upon illumination with 525 nm light.

### Results & discussion

Different sizes and shapes of  $\text{Cu}_{2-x}\text{S}$  NCs are shown in Fig. 1. This was achieved by varying the flow rates from 150  $\mu\text{l}/\text{min}$  (triangular prism with perimeter  $13.5 \times 12.9 \times 11.7$  nm), 1000 to 3000  $\mu\text{l}/\text{min}$  (rod-shaped with aspect ratio 1.3–3.4) and 4000 to 5000  $\mu\text{l}/\text{min}$  (spherical with diameters from 3.6 nm to 8.8 nm). Furthermore, morphological control of the NCs was attained by varying the Cu:S molar ratio from 1:6 and 1:2 (rod-shaped with aspect ratio from 2.3 to 3.4) and 1:10, 2:1, 6:1 and 10:1 (spherical with diameter from 6.4 nm to 12.6 nm). In addition to morphological control, we also observed that the crystal compositions and LSPR spectra were significantly influenced by the Cu:S molar ratio while the flow rates influenced the morphology of nanocrystals significantly. The compositions of  $\text{Cu}_{2-x}\text{S}$  NCs were varied by using different Cu:S molar ratios such as 1:10, 1:6 and 1:2 (covellite,  $x = 1$ ), 2:1 (roxbyite,  $x = 0.25$ ) and 6:1, 10:1 (djurleite,  $x = 0.0625$ ). Correspondingly, different molar ratios resulted in changes in the  $\text{Cu}_{2-x}\text{S}$  stoichiometry,

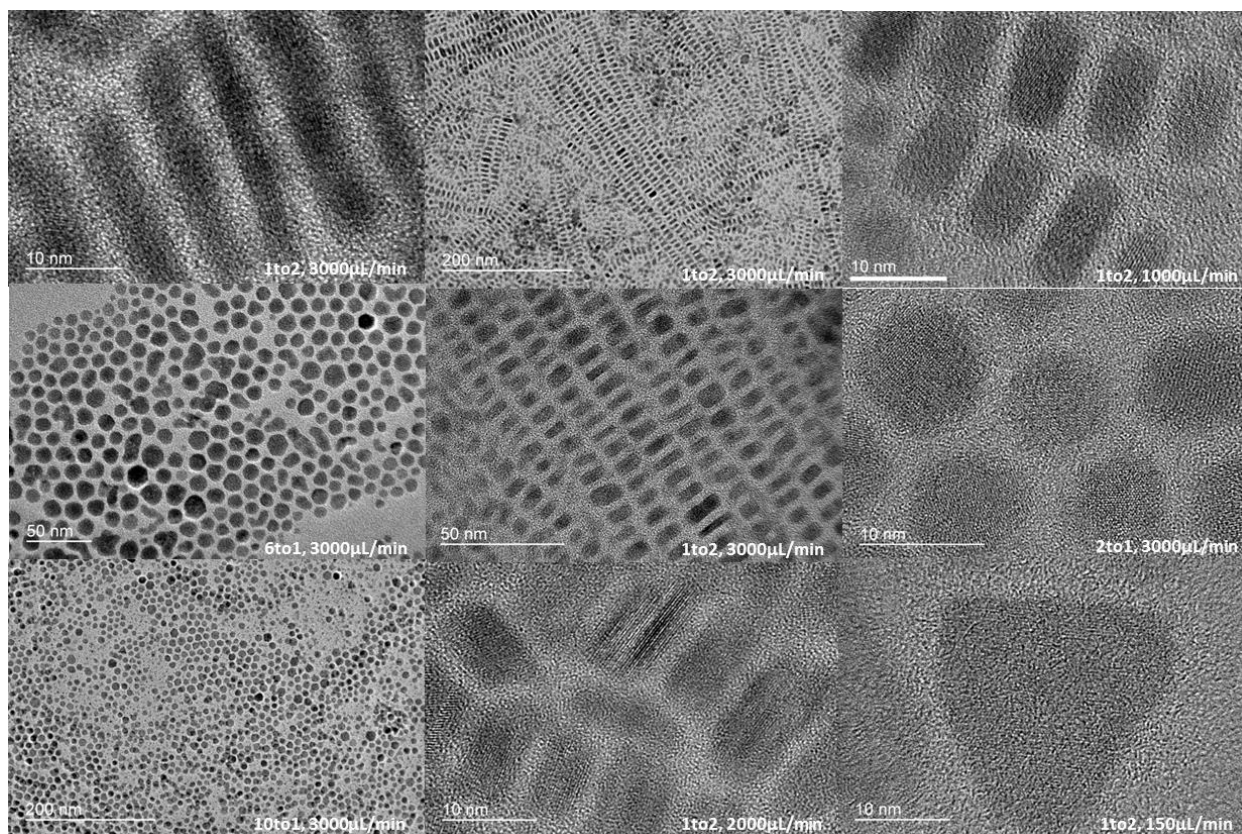


**Fig. 1** TEM images of  $\text{Cu}_{2-x}\text{S}$  NCs synthesized under different flow rates and Cu:S molar ratios.

causing the LSPR peak to shift from 1115 nm to 1644 nm. Table 1 provides a summary of our findings. The  $\text{Cu}_{2-x}\text{S}$  NCs were synthesized using our homemade continuous-flow millifluidic chip as presented in Fig. 2. This device is multifunctional, consisting of four ports (two precursor inlets, an ethanol inlet and an outlet for collection) and housing five different sections as illustrated in Fig. 2a. The precursors first enter the Y-shape region before delivery into the winding section for mixing. The addition of the winding section helps to enhance mixing of the precursors.<sup>27,35</sup> After mixing, the subsequent straight section provides a uniform incubation environment for particle nucleation and growth. Finally, the reaction is quenched by injecting absolute ethanol in the last section of the chip and the synthesized  $\text{Cu}_{2-x}\text{S}$  NCs was collected at the outlet.

The actual nanoparticle fabrication in the continuous-flow device is shown in Fig. 2b. It is obvious that the green color of the solution became darker as it flowed along the 460 mm long channel. Precursors were firstly mixed in the winding section and underwent nucleation in the “Nucleation Section” as shown in Fig. 2a, which corresponded to the light green color solution observed in Fig. 2b. Along the “Growth Section”, the solution became darker and darker, indicating that the growth of particles initiated and the particle size was getting larger. Finally the particles were quenched in the “Quenching Section”.

The geometry of the millifluidic chip is 1.5 mm wide, 1.5 mm deep and approximate 545 mm long. Therefore, the total

volumetric capacity for this chip is 1227 mm<sup>3</sup> or 1227 µl. The total NP fabrication time ranges from approximately 15 s (highest flow rate, 5000 µl/min) to 490 s (lowest flow rate, 150 µl/min). In order to provide uniform heating on each section of the channel, it utilizes a small 76 × 52 mm sized glass slide (Fig. 2c) so that the reaction temperature fluctuations among the particles was minimized. The high surface-to-volume design (Fig. 2d) of the channel enhanced the contact of the particles to the heating plate so that the particles can grow in a homogenous environment within the channel. One of the major advantages of NP synthesis using our homemade continuous-flow device is that it reduced the complexity of the incubation environment as the channels in the chip are enclosed, thus reducing the exposure of the precursors to oxygen. This is unlike traditional macroscale synthesis methods in which the system must be sealed from oxygen by positive pressure of argon/nitrogen gas. Failure of oxygen-sealing would result in oxidation of precursors, especially the high reactive copper precursor. Another important advantage of this chip is the relatively simple passive device which does not involve any moving mechanical components and electrical inputs, unlike other sophisticated micro-electro-mechanical systems.<sup>36</sup> In addition, this millifluidic on-chip fabrication approach promises high reproducibility due to the fixed incubation environment housed within the chip. Due to the small dimensions of the channels, the Reynolds number is low, and hence laminar flow without turbulence can be ensured.<sup>37</sup> This renders mixing in the

**Table 1** Summary of the morphologies, compositions and plasmonic absorption peaks of Cu<sub>2-x</sub>S NCs under different flow rates and copper to sulfur molar ratios.

Molar Ratio (Cu:S)	Flow Rate ( $\mu\text{l}/\text{min}$ )	Shape	Dimension	Aspect Ratio	Throughput Time (s)	Yield (%)	Composition	LSPR Peak (nm)
			AR: Aspect Ratio D: Diameter (nm) L: Length (nm) W: Width (nm) P: Perimeter (nm)					
1:10	3000	Spherical	D: 6.4	$1.2 \pm 0.3$	25	86	Covellite	1115
1:6	3000	Rod	L: 12.0, W: 5.3	$2.3 \pm 0.5$	25	87	Covellite	1150
1:2	3000	Rod	L: 13.9, W: 4.3	$3.4 \pm 1.0$	25	90	Covellite	1272
2:1	3000	Spherical	D: 8.8	$1.1 \pm 0.1$	25	93	Roxbyite	1315
6:1	3000	Spherical	D: 11.9	$1.1 \pm 0.2$	25	94	Djurleite	1471
10:1	3000	Spherical	D: 12.6	$1.1 \pm 0.1$	25	97	Djurleite	1644
1:2	150	Prism	P: 13.5 $\times$ 12.9 $\times$ 11.7	Not Applicable	490	40	Low Yield*	1281
1:2	1000	Rod	L: 7.8, W: 6.2	$1.3 \pm 0.4$	72	91	Covellite	1246
1:2	2000	Rod	L: 12.0, W: 5.3	$2.3 \pm 0.4$	37	87	Covellite	1266
1:2	4000	Spherical	D: 8.8	$1.1 \pm 0.1$	18	78	Spionkopite	1293
1:2	5000	Spherical	D: 3.6	$1.2 \pm 0.2$	15	67	Spionkopite	1277

\*Due to the large variation of crystallinity. No specific conclusion can be drawn.

channels well-controlled and reproducible, minimizing the influence of turbulence induced in the macro-mixing. Thus, this continuous-flow device provides an excellent platform to study reaction dynamics as it enables us to control parameters such as flow rate (absolute or relative), flow regime (continuous or segmented flow) and reaction chamber geometry, which are not accessible in the bench-top system.<sup>38,39</sup> Lastly, less reagents were required in the continuous-flow based synthesis compared to the macroscale synthesis, hence resulting in lesser chemical waste production and reduced environmental impact.<sup>25</sup>

Using the homemade continuous-flow device, a low yield (about 30%) of prism-shaped Cu<sub>2-x</sub>S NCs with an average perimeter 13.5 $\times$ 12.9 $\times$ 11.7 nm was obtained initially under a slow flow rate of 150  $\mu\text{l}/\text{min}$  while fixing the Cu:S molar ratio at 1:2 (Fig. 3a). When the flow rate was increased to 1000  $\mu\text{l}/\text{min}$ , a high yield of spherical particles with shape distribution (aspect ratio  $1.3 \pm 0.4$ ) was obtained (Fig. 3b). With further increase of flowing speed, Cu<sub>2-x</sub>S nanorods with aspect ratios of  $2.3 \pm 0.4$  and  $3.4 \pm 1.0$  were formed at flow rates of 2000  $\mu\text{l}/\text{min}$  and 3000  $\mu\text{l}/\text{min}$  (Fig. 3c and i) respectively. We believed that the growth of the rod-shaped particles could be attributed to prolonged nucleation. At the molecular level, under such high flow rates, the precursor molecules did not have sufficient time to form adequate nuclei. The remaining free precursor molecules could only react and accumulate on the reactive side of the nuclei, resulting in rod-shaped nanocrystals. A similar mechanism for the formation of rod-shaped nanoparticles was also reported by Choi et al. who explained that the morphological variations of the nanocrystals was attributed to the reactive facet binding in a seed-mediated growth mechanism.<sup>40</sup> However, when the flow rate was further

increased to 4000  $\mu\text{l}/\text{min}$  and 5000  $\mu\text{l}/\text{min}$ , the particles became spherical with diameters of 8.8 nm and 3.6 nm (Fig. 3j and k) respectively. Due to the presence of some very small particles which were 2-4 nm in size (diameter), we hypothesize that at flow rates greater than 3000  $\mu\text{l}/\text{min}$  the particles might not have had adequate time to grow and thus could not bind to the reactive side of the nuclei, hence they were unable to sustain the elongated rod-shaped morphology.

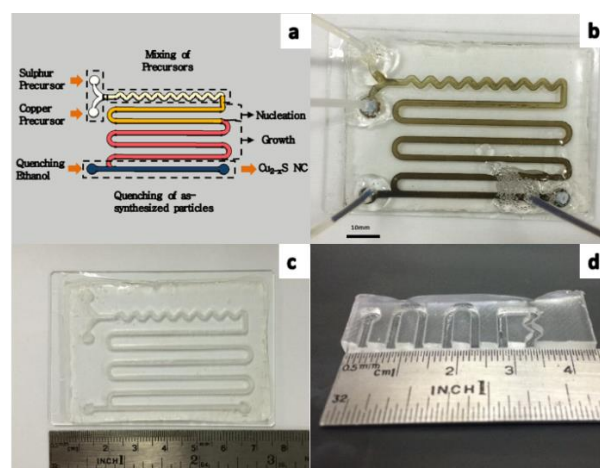


**Fig. 2** (a) Schematic design of continuous-flow millifluidic chip with annotations of different stages of NP formation. (b) Actual PDMS chip for NP fabrication in continuous-flow regime. (c) Top view and (d) cross-sectional view of the actual PDMS chip.

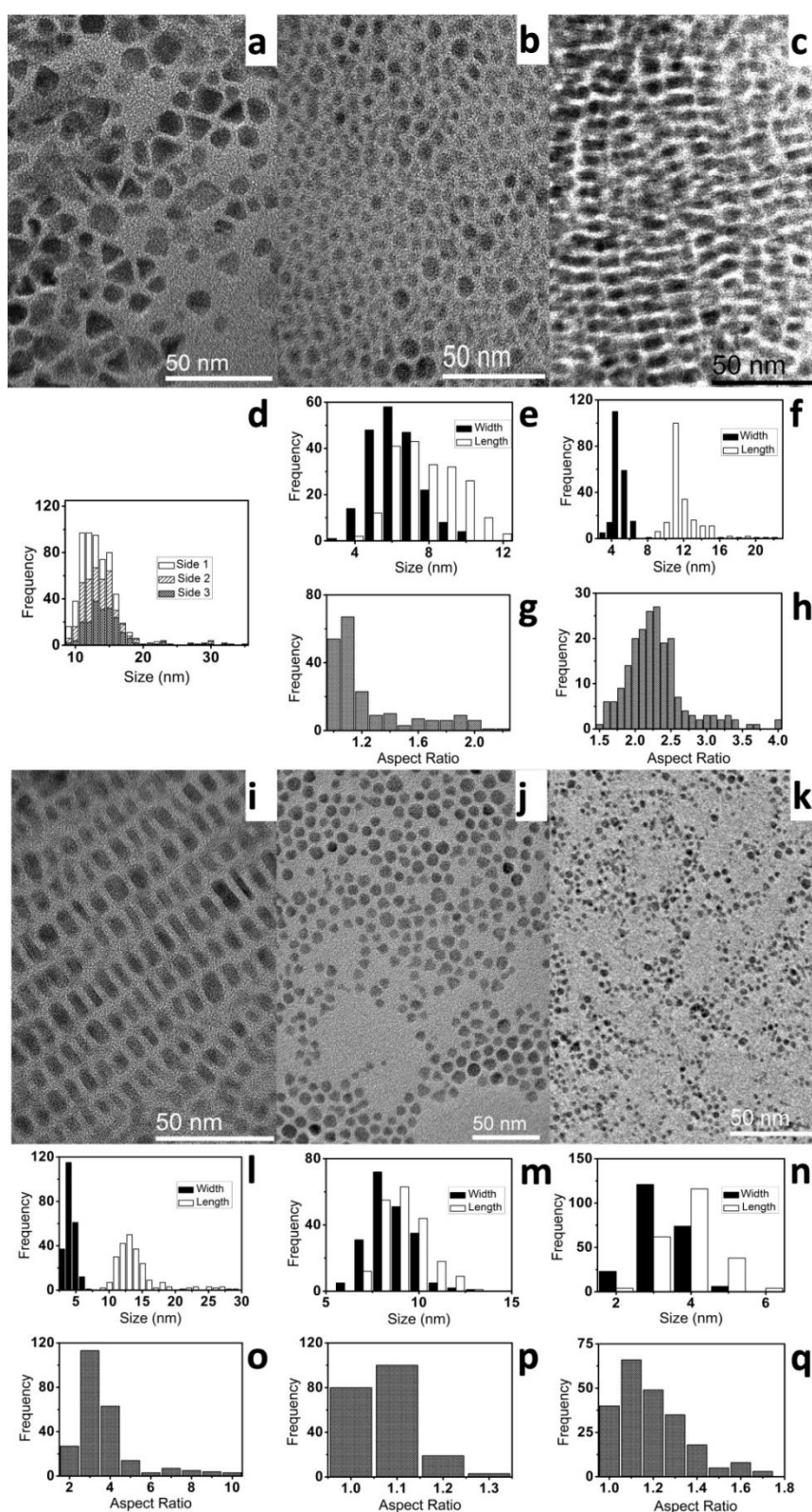


**Fig. 3** TEM images of  $\text{Cu}_{2-x}\text{S}$  NCs exhibiting different morphologies synthesized at flow rates of (a) 150  $\mu\text{l}/\text{min}$ , (b) 1000  $\mu\text{l}/\text{min}$ , (c) 2000  $\mu\text{l}/\text{min}$ , (i) 3000  $\mu\text{l}/\text{min}$ , (j) 4000  $\mu\text{l}/\text{min}$  and (k) 5000  $\mu\text{l}/\text{min}$ , and their respective size distributions (d, e, f, l, m and n) and aspect ratios (g, h, o, p and q). The Cu:S molar ratio was kept at 1:2.

On the other hand, for studying the influence of Cu:S molar ratio under a constant flow rate of 3000  $\mu\text{l}/\text{min}$ , two scenarios were employed. First, when the number of mole of oleic acid-sulfur (OA-S) precursor is larger than the oleylamine-copper (OAm-Cu) precursor (i.e. 1:10), some spherical particles with an aspect ratio of  $1.2 \pm 0.3$  were observed (Fig. 4a). When the concentrations of OA-S decreased to 1:6 and 1:2, rod-shaped nanocrystals with aspect ratios of  $2.3 \pm 0.5$  and  $3.4 \pm 1.0$  were formed respectively. (Fig. 4b and c) In the second scenario, which was the number of mole of OAm-Cu higher than OA-S, the nanocrystals exhibited negligible changes in morphology (Fig. 4j-l) but large variations of the crystal compositions. The crystal composition changed from the original copper-deficient covellite (CuS) (1:2 Cu:S molar ratio) to roxbyite ( $\text{Cu}_{1.75}\text{S}$ ) for 2:1 Cu:S molar ratio. The composition was then further altered to djurleite ( $\text{Cu}_{1.94}\text{S}$ ) for 6:1 and 10:1 Cu:S molar ratios. All these three copper-sufficient precursors exhibited spherical shapes with diameters of 8.8 nm (2:1), 11.9 nm (6:1), and 12.6 nm (10:1 Cu:S molar ratios). The slight variation of shapes observed in different Cu:S molar ratios may be attributed to changes in composition of the nanocrystals which might have affected the binding or caused steric hindrance on the reactive side of the nuclei.

Our results indicated that the flow rates could lead to the changes nanocrystals morphologies, while the lower Cu:S molar ratios have more significant effect on the composition of nanocrystals. Under standard ambient temperature and pressure, the stoichiometric factor in copper sulfide ( $\text{Cu}_{2-x}\text{S}$ ) can span a wide range of values, resulting in forms such as covellite (CuS), anilite ( $\text{Cu}_{1.75}\text{S}$ ), digenite ( $\text{Cu}_{1.8}\text{S}$ ), djurleite ( $\text{Cu}_{1.95}\text{S}$ ), and chalcocite ( $\text{Cu}_2\text{S}$ ).<sup>41</sup> However, using our continuous-flow synthesis chip, additional structures for instance roxbyite ( $\text{Cu}_{1.75}\text{S}$ ) and spionkopite ( $\text{Cu}_{1.39}\text{S}$ ) could be obtained. The variety of copper sulfide nanocrystal compositions could be due to the high pressure conditions provided by the small enclosed environment. In order to identify the composition of the particles, powder samples were characterized using powdered X-ray diffraction (XRD) analysis. Four different kinds of copper sulfide crystal compositions comprising copper-deficient covellite (CuS), spionkopite ( $\text{Cu}_{1.39}\text{S}$ ), roxbyite ( $\text{Cu}_{1.75}\text{S}$ ) and copper-rich djurleite ( $\text{Cu}_{1.94}\text{S}$ ) were elucidated and presented in Fig. 5. The samples with flow rates from 1000 - 3000  $\mu\text{l}/\text{min}$  exhibited major peaks at  $29.25^\circ$ ,  $31.76^\circ$ ,  $32.82^\circ$  and  $47.89^\circ$  (2-theta values) indicating the respective (102), (103), (006) and (110) planes of covellite. The high resolution transmission electron microscope (HRTEM) images in Fig. 6a and c show that the lattice distances of the particles were  $2.815\text{\AA}$  and  $1.898\text{\AA}$  corresponding to the (103) and (110) crystallographic planes of hexagonal covellite (PDF card number 01-078-2391). The FFT analysis (Fig. 6b and d) of these particles also show the agreement of covellite structure. However, the XRD pattern in Fig. 5a for the high flow rates of 4000  $\mu\text{l}/\text{min}$  and 5000  $\mu\text{l}/\text{min}$  did not resemble covellite but matched spionkopite ( $\text{Cu}_{1.39}\text{S}$ ) instead. The pattern exhibited major peaks at  $29.00^\circ$ ,  $32.21^\circ$ ,  $47.57^\circ$  and  $50.08^\circ$  indicating the respective (605), (608), (660) and (6 0 19) planes of spionkopite. Similarly, the lattice distance of  $1.910\text{\AA}$  (Fig. 6k)

refers to the (660) crystallographic plane of the hexagonal spionkopite (PDF card number 00-036-0380). The spionkopite structure was further corroborated by the FFT analysis as depicted in Fig. 6l. When the molar ratio of Cu:S increase, the NCs at 2:1 Cu:S ratio exhibited roxbyite ( $\text{Cu}_{1.75}\text{S}$ ) structure as shown in Fig. 5b. The corresponding XRD pattern shows major peaks at  $26.59^\circ$ ,  $31.20^\circ$ ,  $34.06^\circ$ ,  $46.84^\circ$  and  $48.90^\circ$  indicating the respective (16 0 0), (18 2 1), (20 0 1), (0 16 0) and (886) planes of roxbyite. The lattice distance of  $1.938\text{\AA}$  obtained from Fig. 6i refers to the (0 16 0) crystallographic plane of the monoclinic roxbyite (PDF card number 00-023-0958). The corresponding FFT analysis (Fig. 6j) for the particle also substantiates the same roxbyite structure. Furthermore, when the Cu:S molar ratio was further increased to 6:1 and 10:1, copper-rich djurleite ( $\text{Cu}_{1.94}\text{S}$ ) was formed. The corresponding XRD pattern in Fig. 5b shows major peaks at  $26.27^\circ$ ,  $37.62^\circ$ ,  $46.13^\circ$ ,  $46.31^\circ$  and  $48.65^\circ$  (2-theta values) indicating the respective (004), (804), (046), (080) and (12 0 4) planes of djurleite. The lattice distances of  $1.870\text{\AA}$  and  $2.389\text{\AA}$  obtained from Fig. 6e and g refer to the (12 0 4) and (804) crystallographic planes of the monoclinic djurleite (PDF card number 00-023-0959). The corresponding FFT analysis (Fig. 6f and h) for the individual particles also confirms the djurleite composition.

The  $\text{Cu}_{2-x}\text{S}$  NCs also exhibit near infra-red (NIR) absorbance peaks due to localised surface plasmon resonance (LSPR). The LSPR peaks can be tuned from 1246 nm to 1293 nm and 1115 nm to 1644 nm by varying the input flow rates (Fig. 7a) and the Cu:S molar ratios (Fig. 7b) respectively. These near infra-red (NIR) LSPRs show that the  $\text{Cu}_{2-x}\text{S}$  NCs are highly self-doped (p-type) semiconductor quantum dots with copper-deficient stoichiometric properties as suggested by Alivisatos.<sup>42</sup> The LSPR spectrum is closely related to the stoichiometry of copper (i.e.  $x$ -value of  $\text{Cu}_{2-x}\text{S}$  NCs). A larger value of  $x$  in the  $\text{Cu}_{2-x}\text{S}$  NC introduces more holes in the copper deficient crystal structure, thereby creating more free hole carriers in the nanocrystal. Denser free carriers provide an environment with higher mobility for free charges on the surface to resonate. Therefore an increase in the  $x$ -value, results in shifting of the LSPR peak to a higher resonant frequency (blue-shift). Kriegel and Xie suggested that the LSPR spectrum shift in copper chalcogenide nanocrystals can be manipulated by the oxidation (inducing more holes) and reduction (holes trapping) of  $\text{Cu}_{2-x}\text{S}$  NCs.<sup>43,44</sup> Moreover, Liu et al. revealed that free carrier holes can be trapped by the deprotonated solvents.<sup>45</sup> They showed that the deprotonated oleic acid can trap free holes on  $\text{Cu}_{2-x}\text{S}$  NCs, resulting in red-shifting of the LSPR absorbance peak. Herein, our study has shown that it is possible to obtain a wide LSPR spectra shift of 529 nm (1115 nm to 1644 nm) controlling the Cu:S molar ratios during the synthesis process. Variation of the flow rates exhibited only a slight shift of 47 nm, ranging from 1246 - 1293 nm. This is because when the Cu:S molar ratio was fixed at 1:2, therefore there was not much difference in the degree of copper deficiency and crystal composition. As shown previously in Fig. 5a, the XRD patterns for the NCs synthesized at 1000  $\mu\text{l}/\text{min}$ , 2000  $\mu\text{l}/\text{min}$  and 3000  $\mu\text{l}/\text{min}$  exhibited the similar structures of covellite ( $x = 1$ ) and spionkopite ( $x = 0.6$ ) for 4000  $\mu\text{l}/\text{min}$  and 5000  $\mu\text{l}/\text{min}$ .

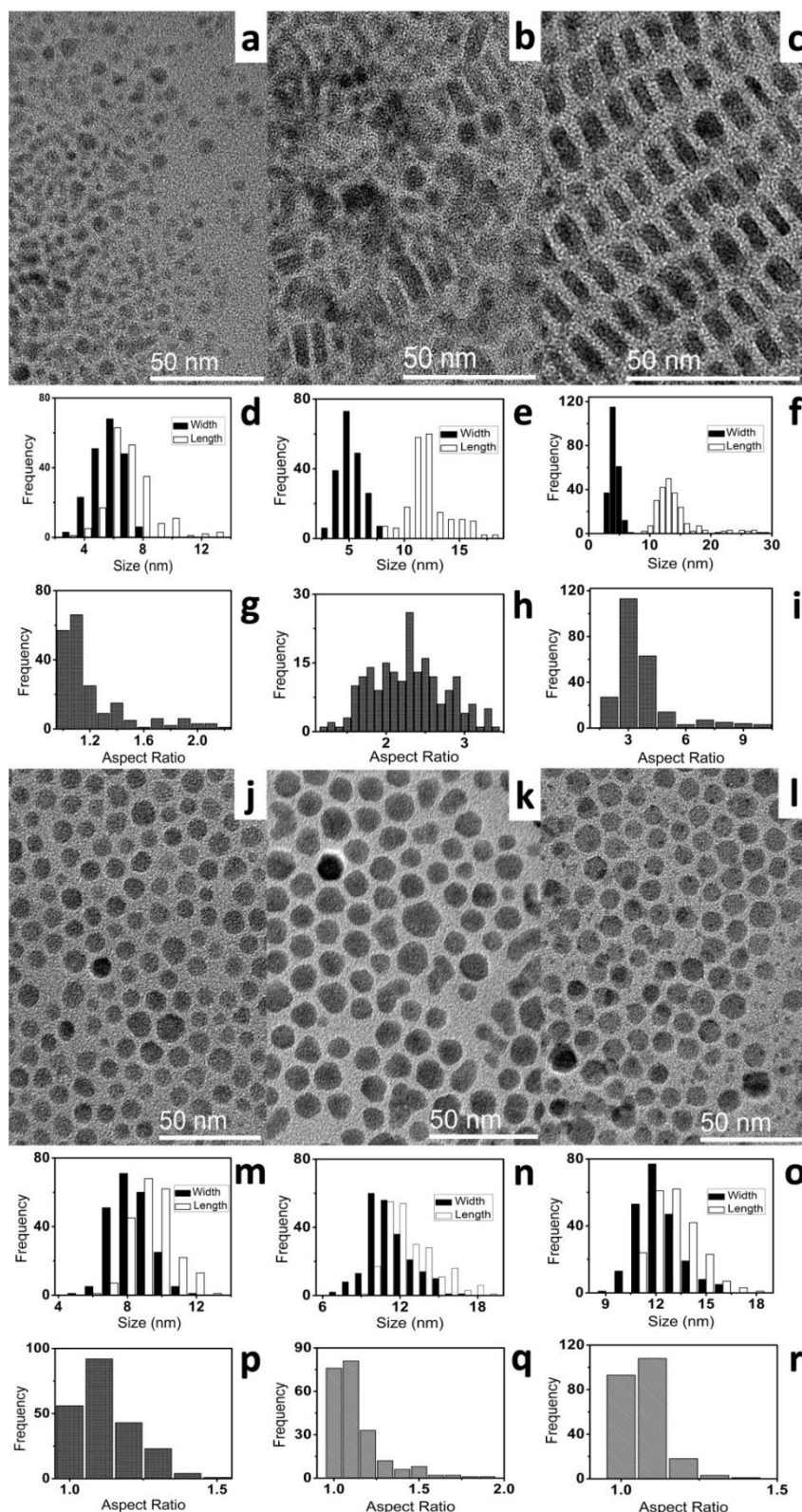


**Fig. 4** TEM images of  $\text{Cu}_{2-x}\text{S}$  NCs synthesizing at different Cu:S molar ratios of (a) 1:10, (b) 1:6, (c) 1:2, (j) 2:1, (k) 6:1 and (l) 10:1, exhibiting different morphologies and their respective size distributions (d, e, f, m, n and o) and aspect ratios (g, h, i, p, q and r). The flow rate was set at 3000  $\mu\text{l}/\text{min}$ .

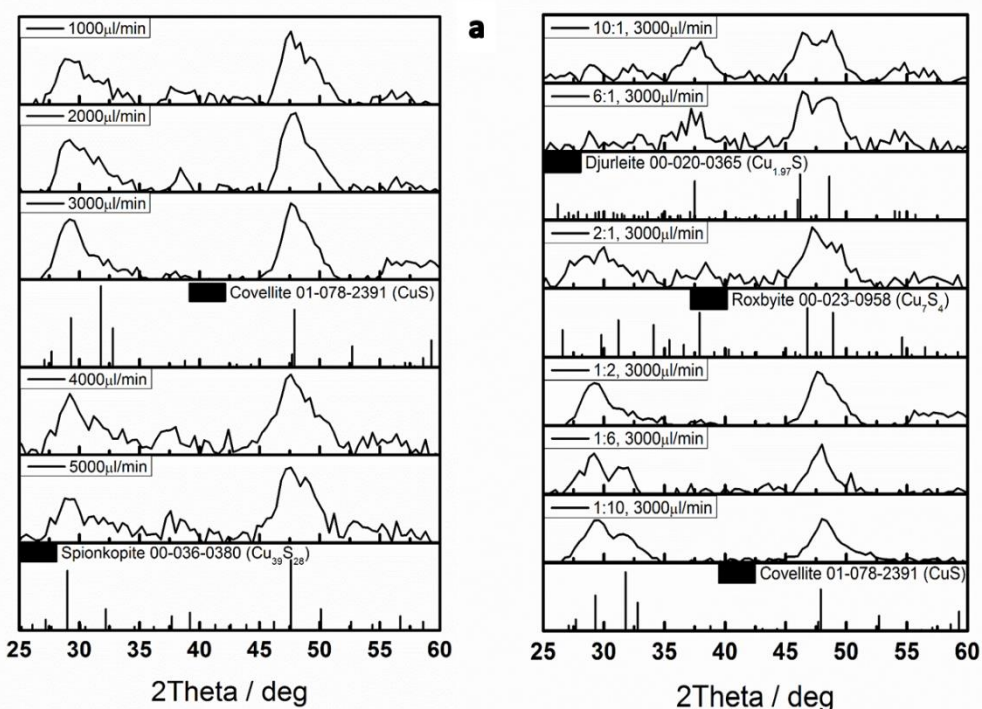


**Fig. 5** Powdered XRD patterns of synthesized  $\text{Cu}_{2-x}\text{S}$  NCs under (a) different flow rates under the same Cu:S ratio (1:2) with the reference pattern of hexagonal covellite (PDF Card 01-078-2391) and hexagonal spionkopite (PDF Card 00-036-0380), (b) different Cu:S molar ratios and the reference pattern of monoclinic djurleite (PDF Card 00-020-0365), monoclinic roxbyite (PDF Card 00-023-0958) and hexagonal covellite (PDF Card 01-078-2391).

Therefore, the LSPR peak shift for the case where only the flow rate was varied could be due to the quantum size effect of  $\text{Cu}_{2-x}\text{S}$  NCs, which were reported by Luther et al. and Saldanha et al.<sup>42,46</sup>

On the other hand, the LSPR peak shift is much more significant with a large shift of 529 nm (1115 nm–1644 nm) (red shift) towards the longer wavelengths with higher Cu:S molar ratios. Oleylamine is a reducing agent which donates electrons to reduce the copper cation.<sup>47</sup> This passivated the hole carriers on the surface of  $\text{Cu}_{2-x}\text{S}$  NCs, thus decreasing the average carrier (hole) density of the nanocrystals and resulting in a red-shift of the LSPR peak.<sup>48</sup> Previously, in Fig. 5b, it was observed that the XRD patterns exhibited the covellite ( $x = 1$ ) composition for 1:2 Cu:S ratio, roxbyite ( $x = 0.25$ ) for 2:1 Cu:S ratio, and djurleite ( $x = 0.06$ ) for 6:1 and 10:1 Cu:S ratios. The corresponding LSPR spectra for these composites red-shifted as the value of  $x$  decreases. This decrease of  $x$  indicates the formation of copper-rich nanocrystals. The red-shift in the LSPR peaks can be attributed to increased passivation of the nanocrystals, which gives rise to lower carrier densities in the crystals as discussed above.

Table 2 consolidates some of the recent work on  $\text{Cu}_{2-x}\text{S}$  NCs, highlighting areas of interest such as the morphology, copper and sulfur precursors, NC dimensions, LSPR peaks as well as parameters studied. To the best of our knowledge, this is first demonstration of continuous-flow organic synthesis of  $\text{Cu}_{2-x}\text{S}$  NCs. Also, our maximum LSPR peak shift of 529 nm is

also one of the widest peak shifts based on the existing literature. In addition, various morphologies were also obtained in this study, which will hopefully provide greater insight for those working in the field. The synthesis protocol adapted in this work was relatively simple and “green” as compared with the conventional approach in which the thiolic and phosphonic ligands (e.g. trioctylphosphine oxide) were involved. Stringent oxygen free environment was required to protect these toxic and easily oxidized during the conventional synthesis.

Photothermal therapy is one of the well-known promising applications of copper sulfide nanoparticles for cancer therapy.<sup>49</sup> It involves the use of near infra-red (NIR) laser light to induce sufficient temperature elevations in tumor cells containing the nanoparticles to induce cell death. The idea behind photothermal therapy is to selectively annihilate the cancerous cells upon the NIR irradiation, leaving the neighboring healthy tissues unscathed, thereby achieving targeted cancer therapy. Currently, gold (Au) nanostructures of various morphologies as well as carbon-based nanomaterials such as carbon nanotubes (CNTs) and graphene have been widely studied as photothermal agents.<sup>50–53</sup>  $\text{Cu}_{2-x}\text{S}$  NCs have only recently emerged as potentially contenders for photothermal therapy due to advantages like cost-effectiveness in terms of synthesis and low cytotoxicity.<sup>54</sup> Besides, the hydrodynamic diameter of GSH capped  $\text{Cu}_{2-x}\text{S}$  NCs ( $6.4 \pm 1.5$  nm) (see supporting information Fig. S1††) was much smaller than the Au nanostructures and CNTs, hence favoring endocytosis and efficient uptake of the

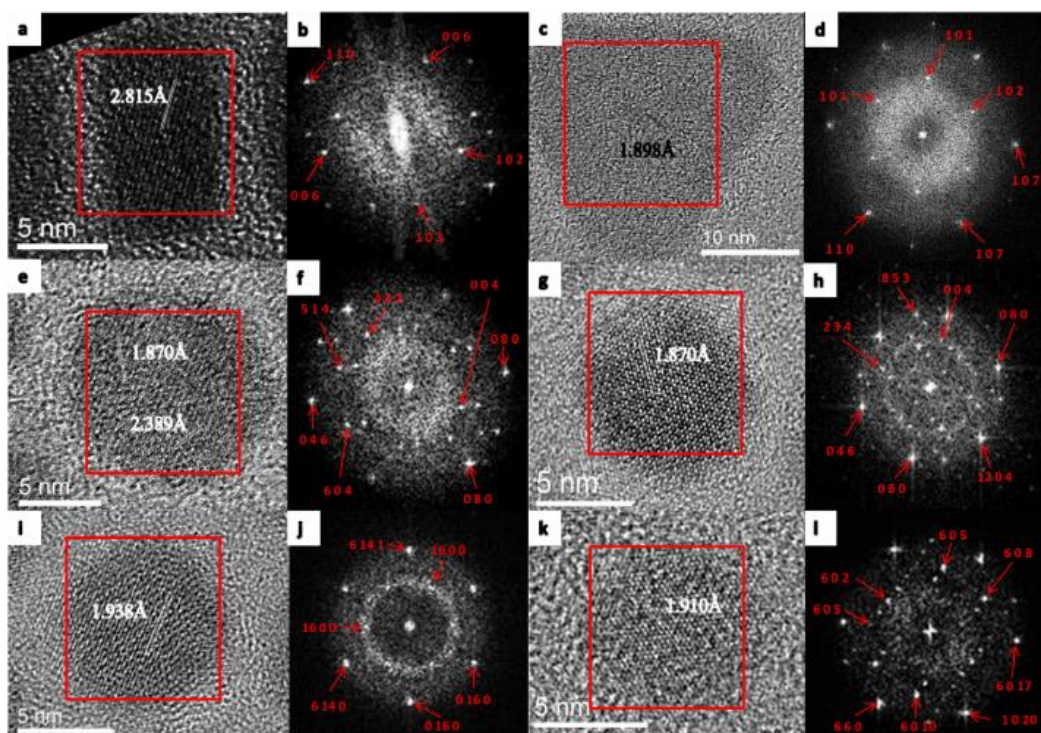


**Fig. 6** HRTEM images of individual nanoparticle for different compositions for covellite (a and c), djurleite (e and g), roxbyite (i) and spionkopite (k), and the corresponding FFT analysis for covellite (b and d), djurleite (f and h), roxbyite (j) and spionkopite (l).

NCs *in vitro* and clearance *in vivo*. In addition, continuous-flow synthesized  $\text{Cu}_{2-x}\text{S}$  NCs have the added edge of reproducibility as the synthesis parameters are better controlled. In this section, we demonstrated a proof-of-concept experiment showing the successful application of GSH capped aqueous phase  $\text{Cu}_{2-x}\text{S}$  NCs in RAW264.7 mice macrophage cell line for photothermal therapy.

Based on the  $\text{IC}_{50}$  value from the MTT (3-(4,5-dimethylthiazol-2-yl)-2,5-diphenyltetrazolium bromide) cytotoxicity assay in (see supporting information Fig. S2††), GSH capped  $\text{Cu}_{2-x}\text{S}$  NC concentrations at  $13.5 \mu\text{M}$  and  $27 \mu\text{M}$  were chosen to investigate the subsequent effect of  $\text{Cu}_{2-x}\text{S}$  NCs as agents for photothermal ablation. A fiber coupled laser diode with center wavelength of  $915 \pm 10 \text{ nm}$  was used as the NIR laser source. The macrophage cells were irradiated with power densities of  $36.7 \text{ W/cm}^2$  and  $52.1 \text{ W/cm}^2$  by varying the laser diode driving current and keeping the beam diameter fixed at around  $1.5 \text{ mm}$ . After laser irradiation, the cells were stained with propidium iodide (PI). PI is a fluorescent dye which is impermeable to the cell membrane of a viable cell and only stains the nuclei of dead or damaged cells which have lost their membrane integrity. Therefore, regions which showed up in red indicate regions of cell death. Despite NIR irradiation at a lower power density of  $21.7 \text{ W/cm}^2$ , no visible cell death was observed, hence we postulate that  $21.7 \text{ W/cm}^2$  was too low for efficient photothermal conversion. Therefore, when the power density was increased to  $36.7 \text{ W/cm}^2$  and  $52.1 \text{ W/cm}^2$ , distinct

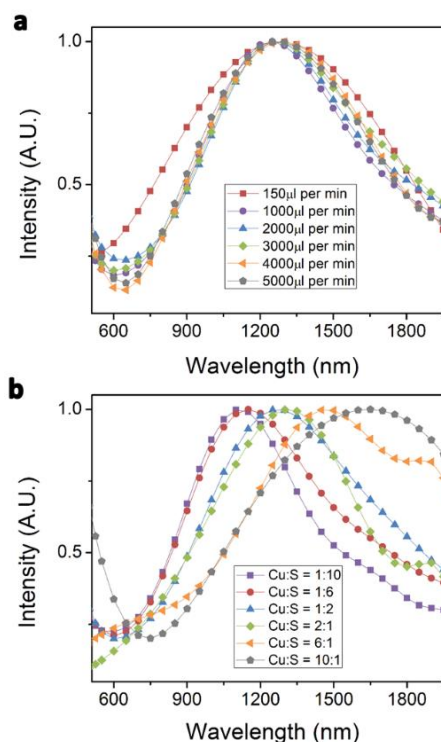


**Fig. 7** UV-VIS-NIR absorption spectra of  $\text{Cu}_{2-x}\text{S}$  NCs obtained with different (a) flow rates and (b) copper to sulfur molar ratios

**Table 2** Brief summary of the synthesis condition, shape and plasmonic absorption of the current Cu<sub>2-x</sub>S semiconductor nanocrystals.

Shape	Synthesis Method	Copper source	Sulfur source	Molar Ratio (Cu:S)	Dimension	LSPR Peak (nm)	Year	Ref.
					AR: Aspect Ratio D: Diameter (nm) L: Lateral (nm) T: Thickness (nm) W: Width (nm) P: Perimeter (nm)			
Disk	Thermolysis	Copper(II) chloride	Postassium (I) ethylxanthate	1:4	L: 15.2 T: 3.8	1130-1260*	2013	55
	Hot Injection	Copper(I) chloride	Sulfur Powder	1:4	L: 13-21 T: 5**	1112-1276**	2013	56
	Solventless Synthesis	Copper nitrate	1-dodecanethiol	1:6	L:24.5 T:4.4	In-plane: 3100 Out-Plane:1800	2011	57
	Thermolysis	Copper nitrate	1-dodecanethiol	1:6	AR: 4.65-7.10*	In-plane: 3100 Out-Plane:1700	2012	58
Hexagonal	Hot Injection	Copper(II) acetylacetonate	ammonium diethyldithiocarbamate	1:1.25	D:5	1250	2012	43
Platelet-like	Heat up Procedure	Copper(I) Chloride	Sulfur Powder	1:2	D: 13-13.7* T: 5-5.3*	1090-1250*	2013	44
Rod	Colloidal Approach	copper acetate	tert-dodecanethiol	1:16	Length: 10-100	NA	2012	59
	Cation Exchange	Cu <sup>+</sup> ions	Sulfur Powder	NA	NA	1128	2013	60
Spherical	Facile Approach	Copper(II) acetylacetonate	Sulfur Powder	2:1	D: 2.8-9.7***	1270-2400*	2014	46
	Hot Injection	Copper(II) acetylacetonate	ammonium diethyldithiocarbamate	1:1.25	D:2-6***	1770	2011	42
	Hot Injection	Copper(I) chloride	Sulfur Powder	1:1	D:6.6-20***	990-1180*	2013	33
	Solventless Synthesis	Copper nitrate	1-dodecanethiol	1:6	D: 4.0	1600	2011	57
	Sono-electrochemical / Hydrothermal	Cupric sulfate	Sodium thiosulfate	1:2	D: 5-20	NA	2009	61
	Hot Injection	Copper(I) chloride	Sulfur Powder	1:2	D: 2.8-13.5	1070-1230**	2013	62
	Non-Injection Approach	Copper(I) chloride	Sulfur Powder	2:1	D: 6.5	1800	2015	63
	Aqueous Synthesis	Copper(I) chloride	Thioacetamide	2:1	D: 2.7-7.2	NA	2015	64
Spherical	Continuous-Flow Millifluidic Synthesis	Copper(I) chloride	Sulfur Powder	1:10 / 2:1 / 6:1 / 10:1	D: 6.4-12.6 <sup>+</sup> D: 3.6-8.8 <sup>^</sup>	1115-1644 <sup>+</sup> 1277-1293 <sup>^</sup>	Our Work	
Rods				1:2 / 1:6	AR: 2.3-3.4 <sup>+</sup> AR: 1.3-3.4 <sup>^</sup>	1150-1272 <sup>+</sup> 1246-1272 <sup>^</sup>		
Prism				1:2	P: 14x13x12	1281		

\*The change is attributed to post-synthesis reactions such as reduction, oxidation or aging.

\*\*The change is attributed to different surfactant or composition molar ratios.

\*\*\*The change is attributed to different synthesis conditions such as reaction time or temperature.

+The change is attributed to different precursor molar ratios.

<sup>^</sup>The change is attributed to different flow rates.

NA: Not Applicable / Not Available.

regions of cell death were observed after staining with PI as depicted in Fig. 8 and Fig. 9. Fig. 8 shows no significant cell death when cells without incubating with Cu<sub>2-x</sub>S NCs were irradiated with NIR laser light. Similarly, no cell deaths were observed in the samples inoculated with 27 μM Cu<sub>2-x</sub>S NCs without laser light irradiation. These results agree with the findings of Li et al.,<sup>54</sup> which also showed no apparent cell death

for cells without neither copper sulfide nanoparticles nor laser illumination. In addition, it can be seen that both the concentration of the Cu<sub>2-x</sub>S NCs as well as the NIR power density played crucial roles in photothermal ablation as relatively well-defined circular regions were observed after the laser treatment (Fig. 9). With the same power density of 52.1 W/cm<sup>2</sup>, the diameter of the region of cell death was 571 μm

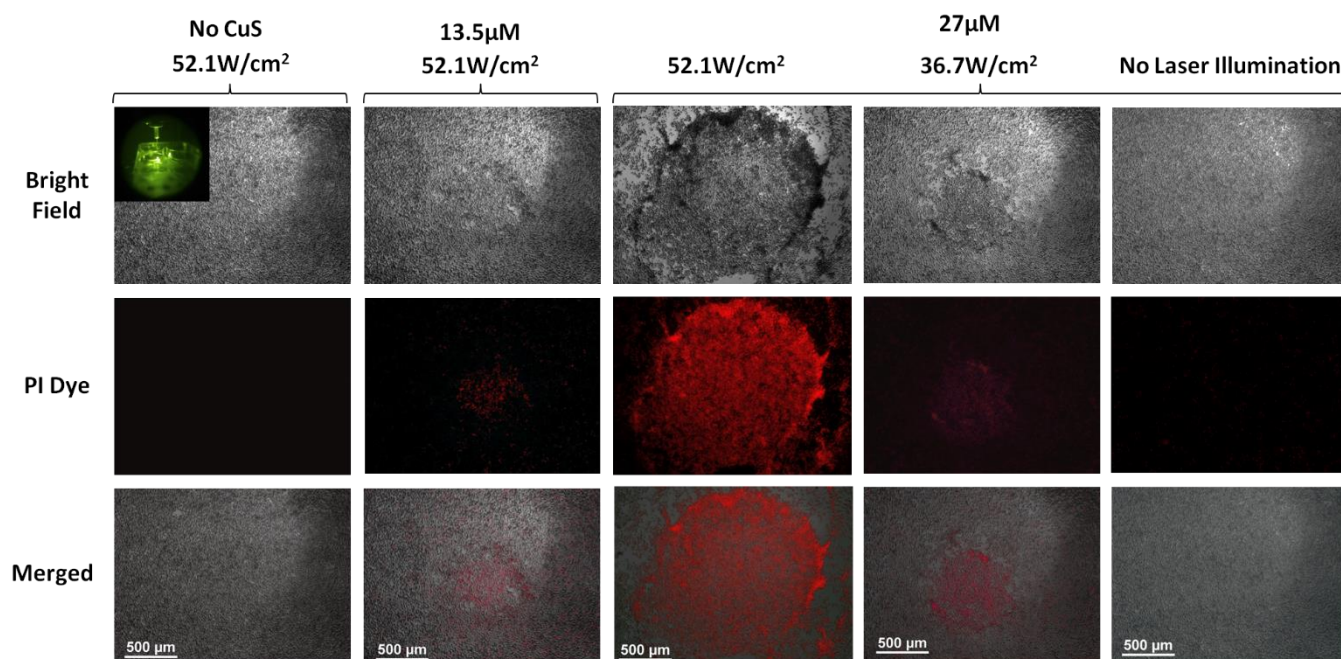


**Fig. 8** Microscope images of RAW264.7 macrophage cells with different  $\text{Cu}_{2-x}\text{S}$  concentrations subjected to NIR illumination at 915 nm at 36.7  $\text{W}/\text{cm}^2$  and 52.1  $\text{W}/\text{cm}^2$  for 15 minutes. Red fluorescence due to cell staining with propidium iodide (PI) indicates regions of cell death or damage. The inset at the top left hand corner shows NIR laser irradiation of cells in the culture well as seen using a NIR viewer.

for the lower diameter of the region of cell death was 571  $\mu\text{m}$  for the lower  $\text{Cu}_{2-x}\text{S}$  NC concentration of 13.5  $\mu\text{M}$  as compared to 1472  $\mu\text{m}$  for the higher 27  $\mu\text{M}$  concentration. This indicates that more extensive cell death could be induced if a higher concentration of NCs was used. However, it should be noted that a balance between the photothermal effect and cytotoxicity of  $\text{Cu}_{2-x}\text{S}$  (MTT assay in supporting information Fig. S2†) should be considered for further biological applications. At a fixed concentration of 27  $\mu\text{M}$ , the higher power density of 52.1  $\text{W}/\text{cm}^2$  resulted in a zone of cell death almost twice in diameter

compared to that of the lower power density of 36.7  $\text{W}/\text{cm}^2$ , spanning 1472  $\mu\text{m}$  and 784  $\mu\text{m}$  respectively as annotated in Fig. 9. This shows that the region of cell death could be enhanced either by increasing the output power of the laser or reducing the diameter of the laser beam. Nonetheless, this may not be desirable for subsequent transition to clinical trials as the power densities are way above the maximum permissible exposure (MPE) limits (0.54  $\text{W}/\text{cm}^2$  for 915 nm).<sup>63</sup> Therefore, superstructures have been engineered to enhance the NIR absorption and photothermal conversion efficiency so that the same photothermal effect can be achieved albeit at much lower power densities near the MPE limit.<sup>66</sup> Alternatively, some groups have proposed the use longer NIR wavelengths in the range of 1000 – 1350 nm because of the advantages of deeper penetration depth and higher MPE ( $\sim 1 \text{ W}/\text{cm}^2$ ) at these wavelengths.<sup>65,67</sup>

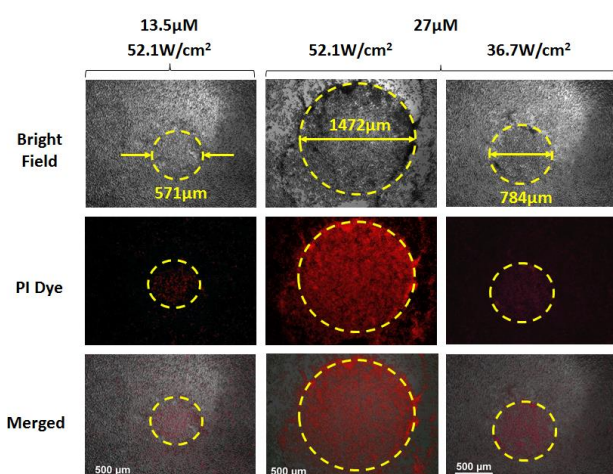


**Fig. 9** Microscope images highlighting regions of cell death induced by NIR irradiation of  $\text{Cu}_{2-x}\text{S}$  NCs and their corresponding sizes with respect to concentration and power density.

## Conclusions

In summary, the input flow rates and copper to sulfide ratios in our continuous-flow microfluidic chip provided substantial control over the shapes and sizes of the  $\text{Cu}_{2-x}\text{S}$  NCs. This surfactant-free approach enabled us to fabricate triangular prism, spherical and rod-shaped NCs with varying aspect ratios by modification of the physical parameters and chemical ratios. Characterizations conducted using TEM, FFT analysis and powdered XRD revealed that the NCs compositions varied from copper-deficient covellite ( $\text{CuS}$ ), spionkopite ( $\text{Cu}_{1.39}\text{S}$ ),

roxybite ( $\text{Cu}_{1.75}\text{S}$ ) to copper-rich djurleite ( $\text{Cu}_{1.94}\text{S}$ ) formation under different synthesis conditions. The LSPR spectra obtained from  $\text{Cu}_{2-x}\text{S}$  NCs were due to the highly self-doped (p-type) semiconductor QDs with copper-deficient stoichiometries. Therefore by varying the Cu:S molar ratios, the LSPR peak could be tuned in the NIR region from 1115 nm to 1644 nm. In addition to the synthesis of  $\text{Cu}_{2-x}\text{S}$  NCs, we have also demonstrated that the photothermal application of these nanoparticles could effectively induce cell death in RAW264.7 mice macrophage cells upon NIR laser irradiation. The continuous-flow millifluidic synthesis chip is a valuable platform for organic synthesis to study the nucleation kinetics of the reactions and offers excellent control over various parameters. We believe that its potential for synthesizing different nanostructures and compositions has not been fully explored. Further investigations on the mechanisms for different shape formation and designs of more advanced functional structures will be carried out in subsequent work.

## Acknowledgements

This work was supported by the Singapore Ministry of Education (Grants Tier 2 MOE2010-T2-2-010 (M4020020.040 ARC2/11) and Tier 1 M4010360.040 RG29/10), NTU-NHG Innovation Collaboration Grant (No. M4061202.040), A\*STAR Science and Engineering Research Council (No. M4070176.040) and School of Electrical and Electronic Engineering at NTU, The Hong Kong Polytechnic University (Project Grant: 1-ZE3A), Research Grants Council (25200914) and National Natural Science Foundation of China (61405169).

## Notes and references

- M. L. Tsai, S. W. Bai and R. H. Chen, *Carbohydrate Polymers*, 2008, **71**, 448-457.
- S. Song, X. Zhou, L. Li and W. Ma, *Ultrasonics sonochemistry*, 2015, **24**, 43-54.
- X. Z. Lin, A. D. Terepka and H. Yang, *Nano letters*, 2004, **4**, 2227-2232.
- J. Wagner and J. Köhler, *Nano letters*, 2005, **5**, 685-691.
- J. Polte, R. Erler, A. F. Thunemann, S. Sokolov, T. T. Ahner, K. Rademann, F. Emmerling and R. Kraehnert, *ACS nano*, 2010, **4**, 1076-1082.
- J. B. Edel and R. Fortt, *Chemical Communications*, 2002, 1136-1137.
- H. Wang, H. Nakamura, M. Uehara, M. Miyazaki and H. Maeda, *Chem. Commun.*, 2002, 1462-1463.
- E. M. Chan, R. A. Mathies and A. P. Alivisatos, *Nano Letters*, 2003, **3**, 199-201.
- M. Mirhosseini Moghaddam, M. Baghbanzadeh, A. Sadeghpour, O. Glatter and C. O. Kappe, *Chemistry-A European Journal*, 2013, **19**, 11629-11636.
- Y. Song, H. Modrow, L. L. Henry, C. K. Saw, E. Doomes, V. Palshin, J. Hormes and C. S. Kumar, *Chemistry of materials*, 2006, **18**, 2817-2827.
- Y. Song, L. L. Henry and W. Yang, *Langmuir*, 2009, **25**, 10209-10217.
- W. Luan, H. Yang, N. Fan and S.-T. Tu, *Nanoscale Research Letters*, 2008, **3**, 134-139.
- H. Wang, X. Li, M. Uehara, Y. Yamaguchi, H. Nakamura, M. Miyazaki, H. Shimizu and H. Maeda, *Chem. Commun.*, 2004, 48-49.
- Y. Song, J. Hormes and C. S. Kumar, *Small*, 2008, **4**, 698-711.
- Y. Li, A. Sanampudi, V. Raji Reddy, S. Biswas, K. Nandakumar, D. Yemane, J. Goettert and C. S. Kumar, *ChemPhysChem*, 2012, **13**, 177-182.
- S. Biswas, J. T. Miller, Y. Li, K. Nandakumar and C. S. Kumar, *Small*, 2012, **8**, 688-698.
- A. A. Hassan, O. Sandre, V. Cabuil and P. Tabeling, *Chemical Communications*, 2008, 1783-1785.
- Y. Li, D. G. Yamane, S. Li, S. Biswas, R. K. Reddy, J. S. Goettert, K. Nandakumar and C. S. Kumar, *Chemical engineering journal*, 2013, **217**, 447-459.
- S. E. Lohse, J. R. Eller, S. T. Sivapalan, M. R. Plews and C. J. Murphy, *ACS nano*, 2013, **7**, 4135-4150.
- J. Huang, L. Lin, Q. Li, D. Sun, Y. Wang, Y. Lu, N. He, K. Yang, X. Yang and H. Wang, *Industrial & Engineering Chemistry Research*, 2008, **47**, 6081-6090.
- H. Jun, T. Fabienne, M. Florent, P.-E. Coulon, M. Nicolas and S. Olivier, *Langmuir*, 2012, **28**, 15966-15974.
- R. Tadmouri, M. Romano, L. Guillemot, O. Mondain-Monval, R. Wunenburger and J. Leng, *Soft Matter*, 2012, **8**, 10704-10711.
- R. Gottesman, A. Tangy, I. Oussadon and D. Zitoun, *New Journal of Chemistry*, 2012, **36**, 2456-2459.
- J.-M. Lim, A. Swami, L. M. Gilson, S. Chopra, S. Choi, J. Wu, R. Langer, R. Karnik and O. C. Farokhzad, *ACS nano*, 2014, **8**, 6056-6065.
- C.-X. Zhao, L. He, S. Z. Qiao and A. P. Middelberg, *Chemical Engineering Science*, 2011, **66**, 1463-1479.
- R. H. Liu, M. A. Stremmer, K. V. Sharp, M. G. Olsen, J. G. Santiago, R. J. Adrian, H. Aref and D. J. Beebe, *Microelectromechanical Systems, Journal of*, 2000, **9**, 190-197.
- H. Song, J. D. Tice and R. F. Ismagilov, *Angewandte Chemie*, 2003, **115**, 792-796.
- A. Jahn, J. E. Reiner, W. N. Vreeland, D. L. DeVoe, L. E. Locascio and M. Gaitan, *Journal of Nanoparticle Research*, 2008, **10**, 925-934.
- F. Trachsel, A. Günther, S. Khan and K. F. Jensen, *Chemical Engineering Science*, 2005, **60**, 5729-5737.
- M. Guo, W.-C. Law, X. Liu, H. Cai, L. Liu, M. T. Swihart, X. Zhang and P. N. Prasad, *Plasmonics*, 2014, **9**, 893-898.
- A. Günther, S. A. Khan, M. Thalmann, F. Trachsel and K. F. Jensen, *Lab on a Chip*, 2004, **4**, 278-286.
- C. Cramer, P. Fischer and E. J. Windhab, *Chemical Engineering Science*, 2004, **59**, 3045-3058.
- L. Liu, H. Zhong, Z. Bai, T. Zhang, W. Fu, L. Shi, H. Xie, L. Deng and B. Zou, *Chemistry of Materials*, 2013, **25**, 4828-4834.
- C. Yang, R. Hu, T. Anderson, Y. Wang, G. Lin, W.-C. Law, W.-J. Lin, Q. T. Nguyen, H. T. Toh and H. S. Yoon, *Journal of Materials Chemistry B*, 2015, **3**, 2163-2172.
- A. Günther, M. Jhunjunwala, M. Thalmann, M. A. Schmidt and K. F. Jensen, *Langmuir*, 2005, **21**, 1547-1555.
- C.-H. Weng, C.-C. Huang, C.-S. Yeh, H.-Y. Lei and G.-B. Lee, *Journal of Micromechanics and microengineering*, 2008, **18**, 035019.
- R. B. Bird, W. E. Stewart and E. N. Lightfoot, *Transport phenomena*, John Wiley & Sons, 2007.
- A. J. Demello, *Nature*, 2006, **442**, 394-402.
- Y. K. Suh and S. Kang, *Micromachines*, 2010, **1**, 82-111.
- S.-H. Choi, E.-G. Kim and T. Hyeon, *Journal of the American Chemical Society*, 2006, **128**, 2520-2521.
- G. Christopher and S. Anna, *Journal of Physics D: Applied Physics*, 2007, **40**, R319.
- J. M. Luther, P. K. Jain, T. Ewers and A. P. Alivisatos, *Nature materials*, 2011, **10**, 361-366.

- 43 I. Kriegel, C. Jiang, J. Rodríguez-Fernández, R. D. Schaller, D. V. Talapin, E. Da Como and J. Feldmann, *Journal of the American Chemical Society*, 2012, **134**, 1583-1590.
- 44 Y. Xie, A. Riedinger, M. Prato, A. Casu, A. Genovese, P. Guardia, S. Sottini, C. Sangregorio, K. Miszta, S. Ghosh, T. Pellegrino and L. Manna, *Journal of the American Chemical Society*, 2013, **135**, 17630-17637.
- 45 X. Liu, X. Wang, B. Zhou, W. C. Law, A. N. Cartwright and M. T. Swihart, *Advanced Functional Materials*, 2013, **23**, 1256-1264.
- 46 P. L. Saldanha, R. Brescia, M. Prato, H. Li, M. Povia, L. Manna and V. Lesnyak, *Chemistry of Materials*, 2014, **26**, 1442-1449.
- 47 S. Mourdikoudis and L. M. Liz-Marzán, *Chemistry of Materials*, 2013, **25**, 1465-1476.
- 48 O. A. Balitskii, M. Sytnyk, J. Stangl, D. Primetzhofer, H. Groiss and W. Heiss, *ACS applied materials & interfaces*, 2014, **6**, 17770-17775.
- 49 S. Goel, F. Chen and W. Cai, *Small*, 2014, **10**, 631-645.
- 50 J. Chen, M. Yang, Q. Zhang, E. C. Cho, C. M. Copley, C. Kim, C. Glaus, L. V. Wang, M. J. Welch and Y. Xia, *Advanced Functional Materials*, 2010, **20**, 3684-3694.
- 51 X. Huang, I. H. El-Sayed, W. Qian and M. A. El-Sayed, *Journal of the American Chemical Society*, 2006, **128**, 2115-2120.
- 52 J. Robinson, K. Welsher, S. Tabakman, S. Sherlock, H. Wang, R. Luong and H. Dai, *Nano Res.*, 2010, **3**, 779-793.
- 53 K. Yang, S. Zhang, G. Zhang, X. Sun, S.-T. Lee and Z. Liu, *Nano Letters*, 2010, **10**, 3318-3323.
- 54 Y. Li, W. Lu, Q. Huang, C. Li and W. Chen, *Nanomedicine*, 2010, **5**, 1161-1171.
- 55 T. Wei, Y. Liu, W. Dong, Y. Zhang, C. Huang, Y. Sun, X. Chen and N. Dai, *ACS Applied Materials & Interfaces*, 2013, **5**, 10473-10477.
- 56 Y. Xie, L. Carbone, C. Nobile, V. Grillo, S. D'Agostino, F. Della Sala, C. Giannini, D. Altamura, C. Oelsner and C. Kryschi, *ACS nano*, 2013, **7**, 7352-7369.
- 57 S.-W. Hsu, K. On and A. R. Tao, *Journal of the American Chemical Society*, 2011, **133**, 19072-19075.
- 58 S.-W. Hsu, W. Bryks and A. R. Tao, *Chemistry of Materials*, 2012, **24**, 3765-3771.
- 59 M. Kruszynska, H. Borchert, A. Bachmatiuk, M. H. Rummeli, B. Büchner, J. r. Parisi and J. Kolny-Olesiak, *ACS nano*, 2012, **6**, 5889-5896.
- 60 I. Kriegel, J. Rodríguez-Fernández, A. Wisnet, H. Zhang, C. Waurisch, A. Eychemüller, A. Dubavik, A. O. Govorov and J. Feldmann, *ACS Nano*, 2013, **7**, 4367-4377.
- 61 Y. Zhao, H. Pan, Y. Lou, X. Qiu, J. Zhu and C. Burda, *Journal of the American Chemical Society*, 2009, **131**, 4253-4261.
- 62 X. Liu, W.-C. Law, M. Jeon, X. Wang, M. Liu, C. Kim, P. N. Prasad and M. T. Swihart, *Advanced Healthcare Materials*, 2013, **2**, 952-957.
- 63 S. Wang, A. Riedinger, H. Li, C. Fu, H. Liu, L. Li, T. Liu, L. Tan, M. J. Barthel and G. Pugliese, *ACS nano*, 2015, **9**, 1788-1800.
- 64 K. Ding, J. Zeng, L. Jing, R. Qiao, M. Jiao, Z. Li and M. Gao, *Nanoscale*, 2015, **7**, 11075-11081.
- 65 L. I. o. America, *Journal*, 2007.
- 66 Q. Tian, M. Tang, Y. Sun, R. Zou, Z. Chen, M. Zhu, S. Yang, J. Wang, J. Wang and J. Hu, *Advanced Materials*, 2011, **23**, 3542-3547.
- 67 X. Ding, C. H. Liow, M. Zhang, R. Huang, C. Li, H. Shen, M. Liu, Y. Zou, N. Gao, Z. Zhang, Y. Li, Q. Wang, S. Li and J. Jiang, *Journal of the American Chemical Society*, 2014, **136**, 15684-15693.